A Reconstruction Method of Detonation Wave Surface

Based on Convolutional Neural Network

Jing Bian [a,b], Lin Zhou [b,c], Pengfei Yang [d], Honghui Teng [a,b,*], Hoi Dick Ng [e]

a. State Key Laboratory of Explosion Science and Technology, Beijing Institute of Technology,

Beijing 100081, China

b. School of Aerospace Engineering, Beijing Institute of Technology, Beijing 100081, China;

c. State Key Laboratory of Laser Propulsion & Application, Beijing Power Machinery Institute,

Beijing 100074, China;

d. SKLTCS, CAPT, BIC-ESAT, Department of Mechanics and Engineering Science, College of

Engineering, Peking University, Beijing 100871, China

e. Department of Mechanical, Industrial and Aerospace Engineering, Concordia University,

Montreal, QC, H3G 1M8, Canada

[*] Corresponding author: hhteng@bit.edu.cn

Abstract：Detonation wave surface is composed of lead shock and reactive front, which are difficult

to be measured simultaneously, so it is necessary to reconstruct the detonation surface. In this study,

a reconstruction method is proposed for predicting lead shock from reactive front to obtain a full

cellular detonation surface. The reconstruction uses a convolutional neural network (CNN) with the

advantages of feature extraction and data dimensionality reduction, and the proposed method has

been verified by data from numerical simulations in this work. The results indicate that this method

performs much better than the traditional multi-layer perceptron (MLP), benefiting from the

advanced architecture of CNN. Furthermore, effects of hyper-parameter choice have been tested,

and the generalization capability of trained CNN for different activation-energy cases are also

discussed.

1. Introduction

Combustion is an important approach for energy conversion, playing a crucial part of energy industry. The industry is exploring a combustion mode with the advantage of high-efficiency and environmental-friendly constantly. A detonation wave is an extreme combustion process with rapid release of energy behind a strong shock wave front. Due to its destructive nature from the severe pressure rise and chemical reaction heat release, the detonation phenomenon has attracted wide interest for safety engineering, terrestrial and astrophysical explosions [1-4]. On the other side, benefiting from its pressure gain and intense energy release, the detonation process has attracted increasing attention for propulsion applications, leading to several types of detonation-based engines [5-11]. These engines have the potential to be a revolutionary technology in aerospace, and their development requires a renewed effort for detonation research to aid interpretation of detonation flow data and unsteady dynamics of detonation in various combustors.

Gaseous detonation waves are inherently unstable, consisting of transverse shocks sweeping across the detonation wave front and thus, forming cellular instabilities. By analyzing the records of triple point trajectories using the smoked foil technique, quantitative measurement of characteristic detonation cell width could intuitively reflect cellular instabilities. The cell width represents a key dynamic parameter and provides a characteristic length scale of detonation wave [12]. Correlation models on the cell width have been proposed to obtain this dynamic parameter with parameters determined from chemical kinetics [13-15]. A recent study also applied the deep

45   artificial neural network approach to develop a model for detonation cell size prediction [16].

46   The traditional experimental techniques used to observe the gaseous detonation dynamics are

47   the smoked foils technique, recording tracks of triple points showing the cellular patterns, and high-

48   speed schlieren photography, visualizing the cellular detonation flow structure. Recently, some

49   advanced optical technologies, such as PLIF (Planar Laser Induced Fluorescence) [17-21] or CTC

50   (Computed Tomography of Chemiluminescence) [22-24], have been developed for combustion

51   diagnosis, which have been employed to examine the inside cellular structure, shedding light on

52   research beyond the cell analysis of static smoked foils. Advanced optical technologies, such as

53   PLIF or CTC, are usually designed to capture the combustion front by capturing

54   a particular transition to deduce the concentration field of a particular species, so schlieren

55   photography is still necessary simultaneously to get the complete wave surface. Furthermore,

56   although CTC has proven its potential to study and reconstruct three-dimensional (3D) flame

57   structures, corresponding 3D shock measurement technology is still not available. To describe fully

58   the unstable cellular detonation structure which composes of both the reaction front and lead shock,

59   a reconstruction method using the information from the combustion measurement is desirable to

60   obtain the lead shock shape and position.

61   Using the basic theory of compressible reaction flow, the parameters of post-shock heat release

62   could be calculated easily given the lead shock and pre-shock conditions. However, the reverse

63   process, i.e. the calculation from the heat release region or flame to the lead shock, cannot be easily

64   achieved to close the coupling. Nowadays, large datasets of detonation flow fields have been

65   generated from numerical simulation and experiments, which provides enough data for AI

66   (Artificial Intelligence) to analyze and figure out the physical laws. Especially for machine learning,

67   whose application is becoming increasingly common in energy field [25-29]. Using machine

68   learning techniques thus provide also a good opportunity to develop a new strategy for detonation

69   modelling. An example is the study reported in [30] for predicting the wave configurations of

70   cellular detonations. The method is based on feedforward artificial neural network (ANN) or the

71   MLP (Multi-Layer Perceptron), but POD (Proper Orthogonal Decomposition) modal analysis is

72   used to extract the features of the flow fields, which in turn becomes involved and requires big data

73   to be accumulated for increasing accuracy. Another preliminary work [31] uses only MLP to

74   construct the detonation surface, demonstrating the MLP performs much better than classic

75   regression methods. However, due to the large number of parameters, the traditional MLP approach

76   is hard to cover the two-dimensional characteristics of the flow field for more accurate

77   reconstruction. Fortunately, CNN (Convolutional Neural Network) has the advantages of parameter

78   sharing and sparsity of connection, and it is expected to provide a solution to detonation wave

79   surface reconstruction with more spatial physics consideration.

80   In this investigation, one new reconstruction method is proposed based on a deep learning-based

81   network, i.e., CNN (Convolutional Neural Network), which is trained to build up the linkage of the

82   lead shock front and reactive front. As a preliminary step, unstable detonations obtained by solving

83   numerically the reactive Euler equations are used to train the CNN, which provides mapping and

84   feedback from the heat release zone to the lead shock. The choice of hyper-parameters and the

85   generalization capability of the proposed CNN approach for reconstructing shock front motion are

86   discussed. The proposed CNN-based shock front reconstruction method is found to be a general

87   method of reconstructing detonation surfaces, and in principle is not restricted by the physical and

88   chemical reaction models used in this work.

2. Datasets and reconstruction method

2.1 Datasets

The structure of two-dimensional (2D) cellular detonations are modeled by the reactive Euler equations with a one-step Arrhenius kinetics and the non-dimensional governing equations are given as follows:

$$\frac{\partial \boldsymbol{U}}{\partial t} + \frac{\partial \boldsymbol{E}}{\partial x} + \frac{\partial \boldsymbol{F}}{\partial y} + \boldsymbol{S} = 0 \tag{1}$$

with

$$\boldsymbol{U} = \begin{bmatrix} \rho \\ \rho u \\ \rho v \\ \rho e \\ \rho \lambda \end{bmatrix}, \boldsymbol{E} = \begin{bmatrix} \rho u \\ \rho u^2 + p \\ \rho u v \\ \rho u(e+p) \\ \rho u \lambda \end{bmatrix}, \boldsymbol{F} = \begin{bmatrix} \rho v \\ \rho u v \\ \rho v^2 + p \\ \rho v(e+p) \\ \rho v \lambda \end{bmatrix}, \boldsymbol{S} = \begin{bmatrix} 0 \\ 0 \\ 0 \\ 0 \\ \dot{\omega} \end{bmatrix}, \tag{2}$$

$$e = \frac{p}{(\gamma - 1)\rho} + \frac{1}{2}(u^2 + v^2) - \lambda Q, \tag{3}$$

$$p = \rho T. \tag{4}$$

$$\dot{\omega} = k\rho(1 - \lambda)\exp(-E_a/T). \tag{5}$$

All flow variables have been made dimensionless by reference to the uniform unburned state ahead of the detonation front,

$$\rho = \frac{\tilde{\rho}}{\tilde{\rho}_0}, p = \frac{\tilde{p}}{\tilde{p}_0}, T = \frac{\tilde{T}}{\tilde{T}_0}, u = \frac{\tilde{u}}{\sqrt{\tilde{R}\tilde{T}_0}}, v = \frac{\tilde{v}}{\sqrt{\tilde{R}\tilde{T}_0}}, Q = \frac{\tilde{Q}}{\tilde{R}\tilde{T}_0}, E_a = \frac{\tilde{E}_a}{\tilde{R}\tilde{T}_0}. \tag{6}$$

The variables ρ, u, v, p, e and Q are the density, velocities in x- and y- direction, pressure, total energy, and the amount of chemical heat release, respectively. For the chemical reaction, λ is the reaction progress variable which varies between 0 (for unburned reactant) and 1 (for product). The reaction is controlled by the activation energy E_a and the pre-exponential factor k, which is chosen to define the spatial and temporal scales. The half-reaction zone length $L_{1/2}$, i.e. the distance required for half the reactant to be consumed in the steady ZND detonation wave, is scaled to unit length,
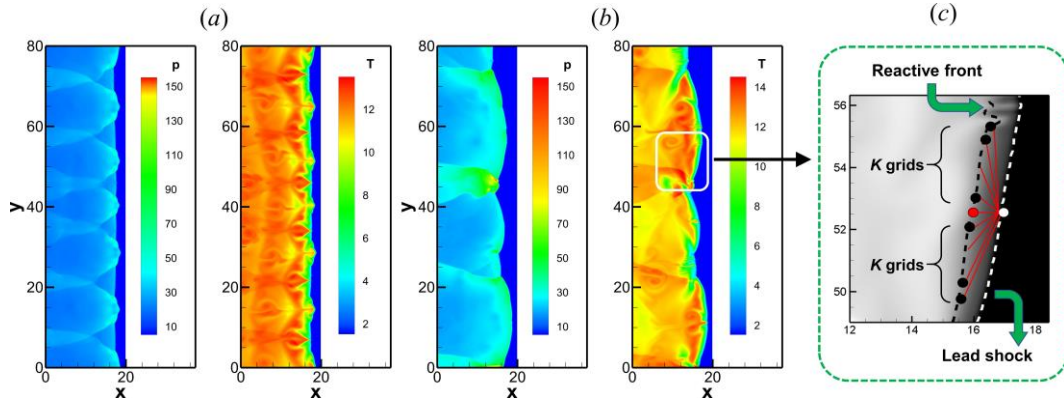
102   which is controlled by pre-exponential factor k with the different E_a [32]. E_a and corresponding k

103   are shown in Table. 1.

104   **Table 1** Pre-exponential factor k used in different cases.

E_a	k
10	3.64
14	6.59
16	8.92
18	12.09
20	16.44
22	22.43
24	30.70
26	42.15

105   Cartesian uniform grids are adopted to discretize the governing equations, which are solved

106   numerically using the MUSCL-Hancock scheme with Strang's splitting [33]. The 2D cellular

107   detonation fields are obtained from the simulation results of detonation wave propagating in a

108   rectangular tube. For the simulation boundary conditions, both the upper and bottom walls of the

109   tube use the slip boundary conditions, while zero-gradient boundary conditions are implemented on

110   the left and the right boundaries. The whole tube is initialized by static unburned gas with unity

111   density and pressure. The ignition zone with high temperature and pressure is used to initiate the

112   detonation, and a self-sustained detonation propagating at nearly Chapman-Jouguet velocity is

113   generated after traveling a certain distance. In the simulations, the dimensionless parameters $Q = 50$

114   and $\gamma = 1.2$ are adopted, which are used traditionally in numerical simulations as canonical values

115   to investigate detonation wave phenomena [34]. About 10 grids per $L_{1/2}$ is used for the following

116   simulations of cellular detonations, which is sufficient to simulate the unstable structures for the

117   activation energy E_a considered in this work. A resolution study on the same results was previously

118   conducted and reported in [31], indicating that this mesh scale is fine enough to reconstruct the

119   shock front. A sufficiently large domain width is set to 80 to ensure enough detonation cells are

120   present. Corresponding to the grid number along y-direction, we get 801 pairs of parameter values

121   for each transient flow field, i.e. one transient detonation field can generate 801 training samples.

Fig. 1 Pressure (left) and temperature (right) fields of cellular detonations with $E_a = 10$ (a) and 20 (b), and schematic diagram of wave surface division (c).

125   The stability of the detonation is sensitive to the activation energy E_a. In this study, the training

126   set is composed of simulation results with $E_a = 10$ or 20, the corresponding CNN is named as E_a-10

127   CNN and E_a-20 CNN, respectively. The pressure and temperature fields with $E_a = 10$ and 20 are

128   shown in Fig. 1. The self-sustained detonations are featured by cellular structures made up of

129   reactive front, lead shock and transverse waves. The interaction between the transverse and lead

130   shock will distort the reactive front and the shock front. This complex dynamic response makes the

131   distance between the reactive front and the lead shock difficult to predict theoretically. In the

132   partially zoomed flow field as illustrated by Fig. 1(c), the black dashed curve represents the reactive

133   front, corresponding to the reaction index $\lambda = 0.5$, while the white dashed curve refers to the shock

134   front, corresponding to the location achieving twice of pre-shock pressure. In essence, the goal of

135   the shock front reconstruction is to predict the location of the white dashed curve according to the

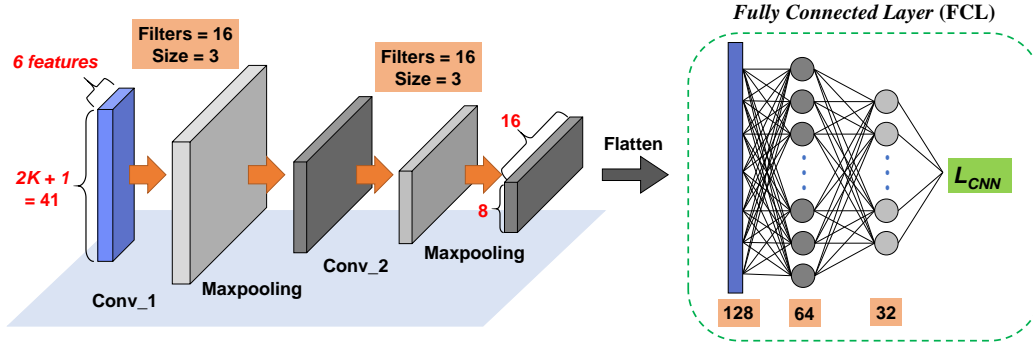136   reactive front parameters of the black one.

137   Numerical results show that the detonation will become unstable and the lead shock front will

138   be more distorted when the activation energy increases to 20. According to our recent study [31],

139   this makes the relation of the shock and reactive front more involved and raises the difficulty to

140   reconstruct the shock. Moreover, only the red circle on the reactive front (black dashed line in Fig.

141   1(c)) is fed as inputs into the multi-layer perceptron in [31], neglecting the effects of the neighboring

142   reactive front on the lead shock. In order to consider the influence of 2D transverse waves on the

143   lead shock, more spatial features on the reactive front should be provided to the neural network.

144   Motivated by this purpose, the wave surface is divided into multiple parts, as shown in Fig.1(c). The

145   white circle on the lead shock front represents the point to be reconstructed. Each sample ensures

146   that there are K grid points above and below the "red point". For this purpose, the grids of reactive

147   front on the upper and lower boundaries are mirrored respectively, so that all points to be

148   reconstructed can still correspond to $2K+1$ input feature grids. The data set consisting of many

149   transient shock-reactive front data is generated from the transient detonation flow fields from

150   simulations. In this study, we use M to denote the number of transient detonation flow fields. For

151   most cases, M is equal to 80. Furthermore, the data set is randomly divided into the training set and

152   validation set, with the ratio 75% and 25%. The validation set can provide a guide for adjusting the

153   CNN architecture and its hyperparameters. In this study, K is equal to 20 in most of the cases. A

154   few cases with different K values aim to test the effects of input grid numbers on the reconstruction.

155 **2.2 CNN architecture and training settings**

156   Due to the input dimension is too large, it is difficult for the traditional MLP method [31] to

157   take the 2D spatial feature of reactive front into account, which may hinder the further optimization

158   of reconstruction results with MLP approach. For CNN, the convolution combined with the pooling

159   operation is an effective method of feature extraction and dimensionality reduction, which makes it

160   feasible to input more spatial features into the neural networks. The CNN architecture in this study

161   contains the convolution part and the fully connected layer (FCL) as shown in Fig. 2. The 2D feature

162   data include six input features on $2K+1$ grid points, i.e. density ρ, temperature T, velocity u, v and

163   corresponding gradients of temperature and density, $T' = \partial T/\partial x$, $\rho' = \partial \rho/\partial x$. These six features have

164   been proven to achieve good reconstruction results for MLP method [31]. Practically, the flame

165   surface information obtained from experiment results are usually very limited and too many input

166   features will cause difficulties in CNN training. More input features may lead to a better

167   reconstruction performance, but it will also increase the difficulty of practical applications. So, this

168   study still uses six major features as input. Convolution layers are set 16 1D convolution kernels

169   with a size of 3 and following a max-pooling layer aim to reduce the dimensionality of the feature

170   maps. Two same convolution-pooling layers form the convolution part. After the convolution part,

171   fewer spatial information and more physical feature combination can be provided for the FCL to

172   reconstruct the shock front. Take $K = 20$ as an example, neuro-computed by the convolution part,

173   the grid point dimension of the data is reduced from 41 to 8, while the feature dimension is increased

174   from 6 to 16, which is conducive to the subsequent prediction of L_{CNN}. Then the 2D feature maps

175   are converted into the 1D vector by the flatten layer and fed into the fully connected layers, which

176   will then figure out the prediction value L_{CNN}, i.e., the distance between the reactive front and leak

177   shock. The FCL is composed of three hidden layers and the number of neurons in each layer is 128,

178   64 and 32, respectively. For different cases, the CNN architecture remains unchanged in this study.

179   A suitable activation function can enhance the nonlinear expression ability of the neural networks.

180 In this study, the activation function all use the LeakyReLU [35], whether for the convolutional

181 layer or the fully connected layer.

182

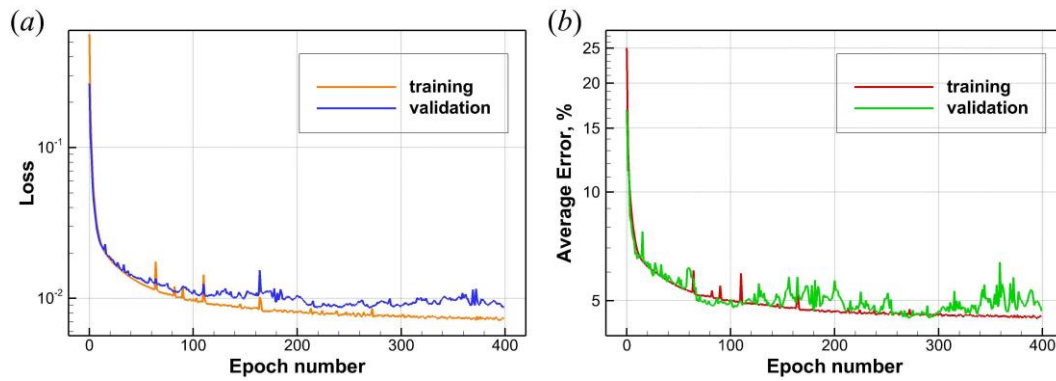183 **Fig. 2** Schematic of the convolutional neural network (CNN).

184 To speed up the training and improve the performance of CNN, normalization of the input data

185 is carried out, which can zero out the mean and normalize the variance. Batch Normalization is

186 applied during each gradient descent, which has been proven to be effective for avoiding the gradient

187 vanishing and the overfitting [36]. The loss function adopts the mean square error (MSE) function

188 as listed in Eq. (7), where N stands for the total number of the training sample. In order to intuitively

189 evaluate the reconstruction accuracy, the relative error between the CNN reconstruction length L_{CNN}

190 and the true distance between shock and reactive front L_{true} is defined as shown in Eq. (8).

$$Loss = MSE = \frac{1}{N}\sum_{i=1}^{N}(L_{true}^i - L_{CNN}^i)^2 \tag{7}$$

$$relative\ error = \frac{L_{CNN} - L_{true}}{L_{true}} \times 100\% \tag{8}$$

191 Training settings often play an important role in the prediction performance of CNN. In this

192 study, we use the Nadam algorithm [37] to perform the gradient descent optimization and update

193 the weight and bias, which is useful to accelerate convergence. For all the neurons and convolution

194 kernels, the weight and bias are initiated by the method by Glorot and Bengio [38], and L2

195 regularization is added to the neurons to avoid overfitting. To check the training effect of CNN, the
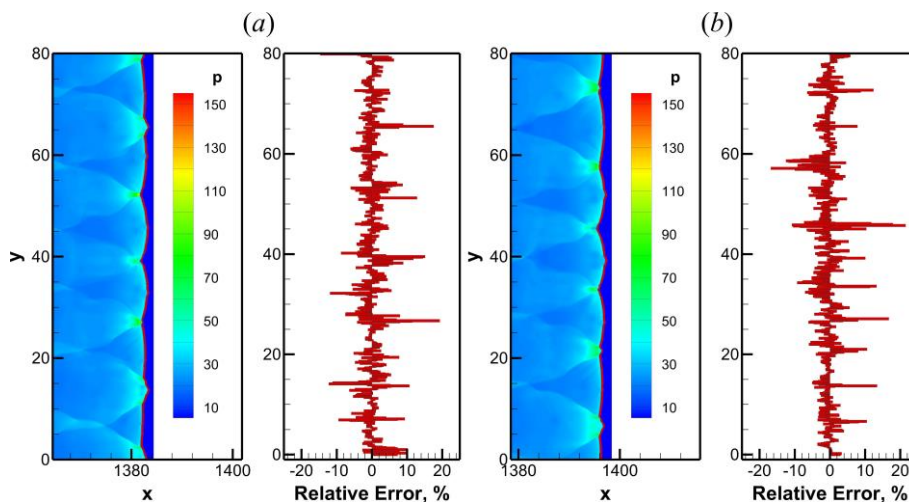
196 average error has been calculated by meaning the absolute value of error on each epoch. Fig. 3

197 demonstrates the loss value and average error in each epoch of the E_a-20 network. The results

198 demonstrate that the loss function has converged to a quite small value after 400 epochs. On the

199 other hand, the learning curve of the training set and validation set almost overlap, indicating that

200 there is hardly any overfitting phenomenon for the training process.

201

202 **Fig. 3** Loss (a) and error (b) curve of the E_a-20 CNN.

203

3. Results and discussion

3.1 Basic reconstruction results

206

207 **Fig. 4** Reconstructed shock (red curve in pressure field) and relative error of shock distance with

208 $E_a = 10$ (a) $t = 85$, (b) $t = 90$.

209 For testing the reconstruction performance of CNN, the test data used consists of transient

210   detonation flow fields at the later moments, which is independent of the training & validation set.

211   Typical reconstruction results from the test set for the cases of $E_a = 10$ are shown in Fig. 4. It is

212   observed that the reconstructed shock, plotted by the red curve in the flow fields, locates around the

213   simulated lead shock, demonstrating that a well-trained CNN can predict the shock shape influenced
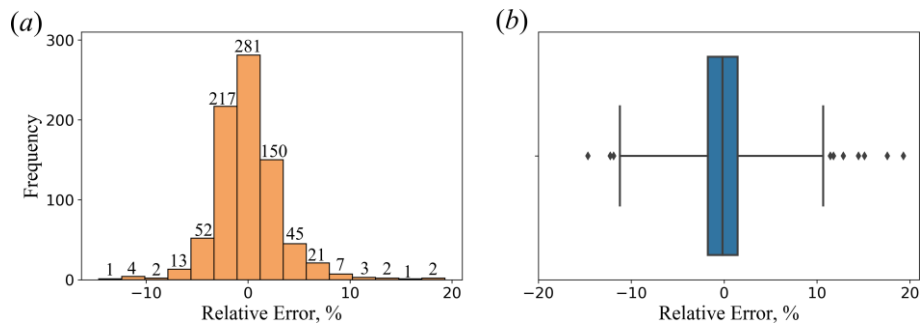
214   by the reactive front precisely. Results of two different instants are displayed with different locations

215   of transverse waves, and both of them illustrate good reconstruction result. The error is below 5%

216   at most part of the surface, and the large errors usually appear, at where the transverse waves collide

217   with each other. For the reconstructed detonation surfaces of Fig. 4, the mean relative errors are

218   2.25% and 2.35%, demonstrating good performance in predicting the shock distance.

219

220   **Fig. 5** Relative error of shock distance with $E_a = 10$, $t = 85$ (a) relative error frequency distribution
221   histogram, (b) boxplot.

222   According to the statistical results, more than 600 results among 801 pairs of data have an

223   absolute value of the relative error of less than 3.5%. The boxplot of Fig. 5(b) shows the dispersion

224   and skewness of the error data through their quartiles. Where, quantile refers to arrange all values
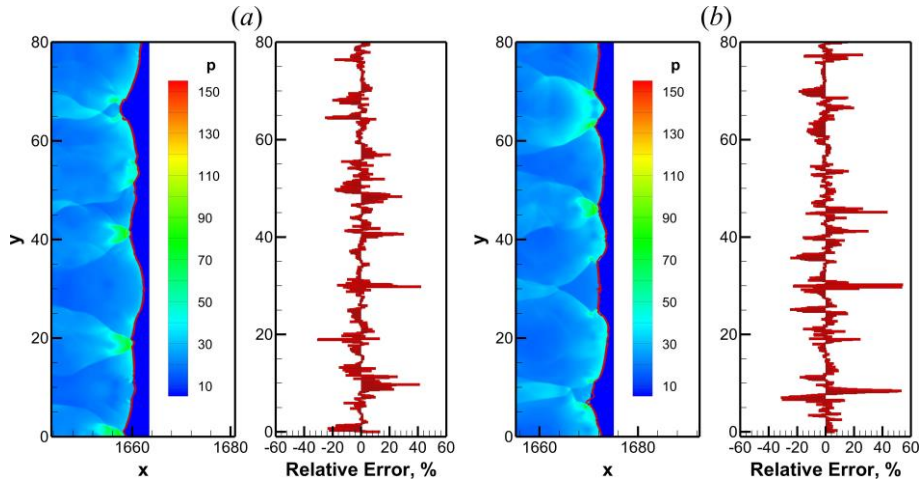
225   from small to large and divide them into four equal parts. The value at the position of three dividing

226   points are called quartile, marked as q_1, q_2, q_3. The upper and lower boundaries of box are
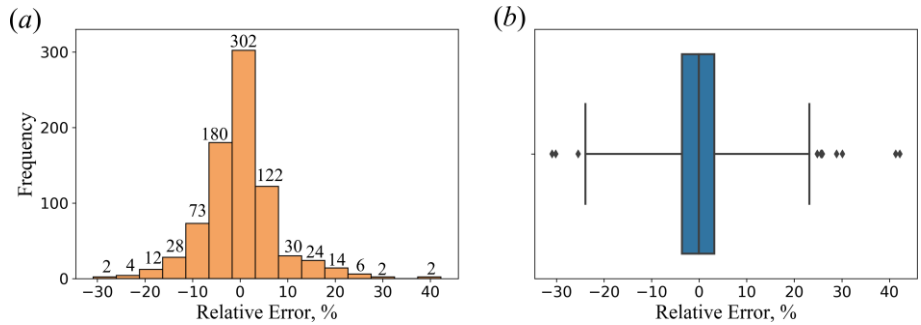
227   determined by q_1 and q_3 respectively and the outliers are set to be less than $q_1 - 3\Delta q$ or more than

228    $q_3 + 3\Delta q$ in this study. Fig. 5(b) indicates the box is quite narrow, revealing that the error data is

229 concentrated in a small range. On the whole, the outliers are mostly within ±20%, which still

230 supports the reasonable performance of this CNN-based reconstruction approach.

232 **Fig. 6** Reconstructed shock (red curve in pressure field) and relative error of shock distance with

233 $E_a = 20$ (a) $t = 85$, (b) $t = 90$.

235 **Fig. 7** Relative error of shock distance with $E_a = 20$, $t = 85$ (a) relative error frequency distribution

236 histogram, (b) boxplot.

237 Typical reconstruction results from the test set for the cases of $E_a = 20$ are shown in Fig. 6 and

238 the corresponding relative error of Fig. 6(a) is shown in Fig. 7. Due to increased activation energy,

239 the detonation surface becomes more unstable, with curved shock and less but strong transverse

240 waves. Generally speaking, the well-trained CNN can predict the shock precisely, although the

241 magnitude of reconstruction error increases compared with the results with $E_a = 10$. The averaged

242 relative errors are 5.25% and 6.03% in Fig. 6(a) and 6(b), respectively. Similar to the last case, a

243 large error appears, at where the transverse waves collide. In future investigation, adding the

244   gradient along *y*-axis as an input feature may be helpful to reduce these local errors. Like the results

245   of $E_a = 10$, most of the errors are concentrated in a small interval (within ±5%). In contrast to E_a-10

246   networks, however, the outliers and the quartiles of E_a-20 networks reconstruction error are larger,

247   indicating that the error data of $E_a = 20$ is more dispersed.

3.2 Effects of hyper-parameter choice

249   The results in Sec. 3.1 are obtained by the default hyper-parameters, i.e. $M = 80$ and $K = 20$,

250   which represent the number of input transient flow fields and the number of input grid points,

251   respectively. The number of training data often plays a crucial role in the prediction performance of

252   CNN. To assess the effect of the training set size, a comprehensive study has been carried out to

253   ensure that 80 transient flow fields are enough to make the CNN achieve a good performance. The

254   number of transient flow fields in the training & validation set, i.e. *M*, varies from 40 to 100 and the

255   corresponding average reconstruction errors are listed in Table 2. The results show that the

256   reconstruction error does decrease with larger *M*. But when *M* increases from 80 to 100, the

257   reconstruction error changes little, indicating that $M = 80$ is sufficient to make CNN achieve

258   satisfactory performance.

259   **Table 2** Average reconstruction errors for $E_a = 20$ in the cases of different *M*.

M	Average error
40	10.16%
60	7.24%
80	5.79%
100	5.45%

260   The robustness of hyper-parameters is also a critical factor for the application and the

261   promotion of CNN. Another parameter *K*, the number of input grid points is also an important hyper-

262 parameter to be discussed, corresponding to the spatial scale of the features provided to the CNN.

263 K is set to 20 in the previous cases, i.e. feeding the feature on $2K+1 = 41$ grids into CNN. Here we

264 change the value of $2K+1$ from 21 to 81. To facilitate comparison with the previous results, the

265 architectures of convolution part and fully connected layers keep the same as mentioned by Sec. 2.2,

266 although different K values will change the total amount of CNN training parameters. Then, the

267 CNNs are trained and tested through the same settings as mentioned above. The average errors of
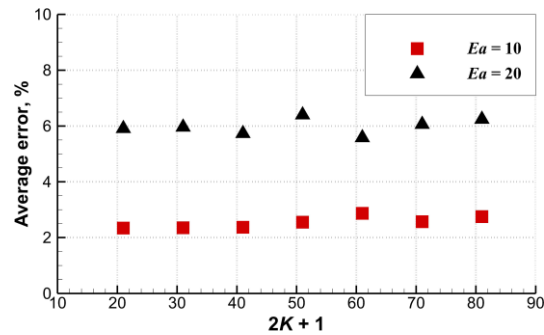
268 reconstruction results are shown in Fig. 8. What stands out in this figure is the insensitivity of

269 reconstruction error to the different values of K. Regardless of $E_a = 10$ or 20, the reconstruction

270 errors only fluctuate in the range of 0.8% while $2K+1$ varies from 21 to 81. These results show that

271 the CNN is robust for the selection of K, which further supports the application of this CNN-based

272 reconstruction approach.

273

274 **Fig. 8** Error of reconstruction results with different K.

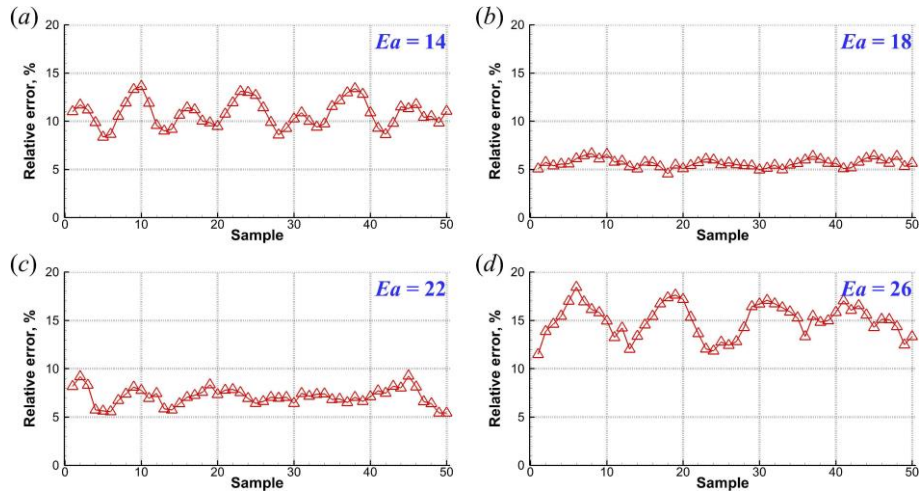## 3.3 Generalization for reconstruction at different activation energies

276 The primary problem of shock front reconstruction based on CNN is the generalization

277 capability. Although a well-trained network can accurately reconstruct the lead shock surface given

278 a fixed activation energy E_a, further tests should be performed to examine the generalization
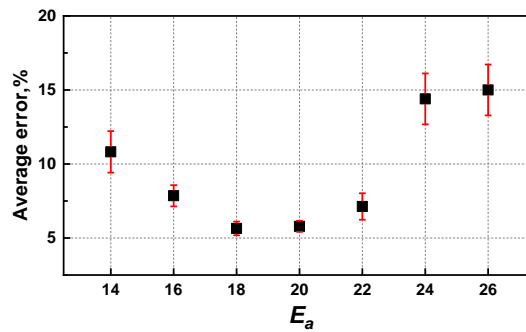
279 capability at different activation energies, which may vary in practical applications. If the proposed

280   method is robust in the lead shock reconstruction for different activation energies, it will be a flexible

281   and powerful tool for future application on shock front reconstruction for detailed chemical

282   reactions based numerical simulation and experimental results.

283

284   **Fig. 9** Error of reconstruction results of four different E_a test set.

285

286

287   **Fig. 10** Average reconstruction errors and standard deviation in the cases of each E_a.

288   Based on the well-trained CNN with $E_a = 20$, the shock front with six other activation energies,

289    $E_a = 14, 16, 18, 22, 24, 26$, are reconstructed. The test set for each E_a has consisted of 50 different

290   transient flow fields extracted from different instants, and the testing results are shown in Fig. 9. For

291   different samples of each E_a, the relative error fluctuates around a mean value. The mean value and

292   the standard deviation of error for each E_a have been plotted in Fig. 10. Generally speaking, the

293   relative error increases when E_a deviates from 20, the activation energy used to train the CNN. In

294 the cases of E_a = 16~22, all the error points locate below 10% and the average errors are less than

295 8%. In contrast, the errors are relatively higher and more scattered in the cases of E_a = 14, 24 and

296 26. Especially for the last two high activation energy flow fields, the average errors have a noticeable

297 growth as shown in Fig. 10. This should be attributed to the fact that the mapping relationships

298 between the reactive front and the corresponding lead shock are very sensitive to E_a. For the high

299 E_a flow fields, the detonation waves are more unstable, which raises the difficulty to reconstruct the

300 shock. But in general, from the perspective of reconstruction error, the well-trained CNN still has a

301 certain generalization ability for flow fields with different activation energies.

302 **Table 3** Testing results of same E_a as training set by CNN and MLP.

	MLP	CNN
E_a-10	4.10%	2.37%
E_a-20	7.04%	5.79%

303 **Table 4** Generalization testing results of each E_a by CNN and MLP based on E_a = 20.

	MLP	CNN
E_a = 14	10.83%	10.82%
E_a = 16	8.77%	7.86%
E_a = 18	7.72%	5.65%
E_a = 22	7.09%	7.13%
E_a = 24	10.21%	14.40%
E_a = 26	12.54%	14.98%

304 In Ref. [31], the multi-layer perceptron (MLP) with two hidden layers is used to reconstruct

305 the shock surface. Compared with the results of the MLP approach [31], CNN has a better

306 reconstruction performance. For the cases of E_a = 10 and E_a = 20, i.e. the E_a of testing sets are the

307 same as the training set, the average reconstruction error reduced by nearly two percentage points

308 as listed in Table 3. This should be attributed to the principle superiority of this CNN-based approach,

309 which covers the impacts of the reactive front on the neighboring lead shock instead of only the lead

310   shock exactly ahead on MLP methods. Meanwhile, the convolution layer with the advantage of

311   feature extraction is also a contributing factor for better prediction performance. Table 4

312   demonstrates the generalization testing results of other E_a by CNN and MLP based on $E_a = 20$. The

313   results reveal that CNN has better generalization performance for flow fields with lower E_a, but

314   there is a greater error for the cases with higher E_a whose mechanism is still unclear. Generally

315   speaking, the CNN approach has better prediction performance and considerable generalization

316   capability compared with the MLP method, which is more promising for future application on the

317   reconstruction for detailed chemical reactions based numerical simulations or even experimental

318   results.

319

4. Concluding remarks

321   A reconstruction method based on CNN has been proposed and tested through 2D numerical

322   results of cellular detonations. The reactive front features are used as input variables and the lead

323   shock location is regarded as the output of CNN. With the help of reasonable data sets and advanced

324   training methods, the proposed method based on CNN demonstrates satisfactory performance to

325   predict lead shock evolution from details of the reactive front. The testing results show that the well-

326   trained CNN is able to reconstruct the position of the leading shock front with a quite low relative

327   error. For E_a-20 CNN, the effects of training data size are also studied by analyzing the testing error

328   of well-trained CNN. A hyper-parameter discussion on the number of input grids, i.e. K, is also

329   carried out. The reconstruction results reveal that this CNN-based approach is robust to the selection

330   of the hyperparameter K.

331   This present method works and performs better than the previous classical MLP method. This

332   should be attributed to the principle superiority of the CNN formulation, which feeds details of the

333   neighboring reactive front into the neural network, instead of just considering the features of the

334   reactive front exactly ahead of the lead shock. For detonations with two activation energy values,

335   compared with the results from the MLP method, the CNN-based approach makes the reconstruction

336   error reduced by nearly 2%. Meanwhile, the well-trained CNN still has a certain generalization

337   capability for detonation flow fields with different activation energies, although the improvement in

338   generalization performance is quite limited compared to the MLP method.

339   The method could be extended to use in other circumstances, providing a new modelling tool

340   for detonation research. This shock reconstruction method is universal and expandable. It should

341   not be limited to 2D, but capable of reconstructing 3D shock. Certainly, for the application to 3D

342   shock reconstruction, detailed chemical reactions based numerical simulations, and even the

343   experimental results, it should depend on more comprehensive and detailed data sets and other

344   advanced technologies in machining learning. This should be further considered in the future

345   research.

346 # Acknowledgement

349 # References

[1] E.S. Oran, Understanding explosions - from catastrophic accidents to the creation of the Universe, Proc. Combust. Inst. 2015; 35: 1-35.

[2] B. Zhang, H. Liu, Y. Li, The effect of instability of detonation on the propagation modes near the limits in typical combustible mixtures, Fuel 2019; 253: 305-310.

[3] B. Zhang, X. Chang, C. Bai. End-wall ignition of methane-air mixtures under the effects of CO2/Ar/N2 fluidic jets. Fuel 2020; 270: 117485.

[4] B. Zhang, Y. Li, H. Liu. Analysis of the ignition induced by shock wave focusing equipped with conical and hemispherical reflectors. Combust Flame 2022,236:111763.

[5] K. Kailasanath, Review of propulsion applications of detonation waves, AIAA J. 2000; 38: 1698-1708.

[6] P. Wolański, Detonative propulsion, Proc. Combust. Inst. 2013; 34: 125-158.

[7] F.A. Bykovskii, S.A. Zhdan, Current status of research of continuous detonation in fuel-air mixture (Review), Combust. Expl. Shock Waves 2015; 51: 21-35.

[8] D. Schwer, K. Kailasanath, Numerical investigation of the physics of rotating-detonation-engines, Proc. Combust. Inst. 2011; 33: 2195-2202.

[9] R. Zhou, D. Wu, J. Wang, Progress of continuous rotating detonation engines, Chin. J. Aero. 2016; 29(1): 15-29.

[10] J.Z. Ma, M.Y. Luan, Z.J. Xia, J.P. Wang, S.J. Zhang, S.B. Yao, B. Wang, Recent progress, development trends, and consideration of continuous detonation engines, AIAA J. 2020; 58(12): 4976-5035.

[11] B. Zhang, Y. Li, H. Liu. Ignition behavior and the onset of quasi-detonation in methane-oxygen using different end wall reflectors. Aerospace Science and Technology 2021; 116:106873.

[12] J.H.S. Lee, Dynamic parameters of gaseous detonations, Ann. Rev. Fluids Mech. 1984; 16:

311-336.

[13] C.K. Westbrook, P.A. Urtiew, Chemical-kinetic prediction of critical parameters in gaseous detonations, Proc. Combust. Inst. 1982; 19: 615-623.

[14] A.I. Gavrikov, A.A. Efimenko, S.B. Dorofeev, A model for detonation cell size prediction from chemical kinetics, Combust. Flame 2000;120: 19-33.

[15] H.D. Ng, Y. Ju, J.H.S. Lee, Assessment of detonation hazards in high-pressure hydrogen storage from chemical sensitivity analysis, Int. J. Hydrogen Energy 2007; 32: 93-99.

[16] K. Malik, M. Zbikowski, A. Teodorczk, Detonation cell size model based on deep neural network for hydrogen, methane and propane mixtures with air and oxygen, Nuclear Eng. Tech. 2019; 51(2): 424-431.

[17] F. Pintgen, C.A. Eckett, J.M. Austin, J.E. Shepherd, Direct observations of reaction zone structure in propagating detonations, Combust. Flame 2003;133: 211-229.

[18] S.W. Grib, C.A. Fugger, P.S. Hsu, N. Jiang, S.Roy, S.A. Schumaker, Two-color OH PLIF thermometry in a detonation channel, AIAA Scitech 2021 Forum, 11–15 & 19–21 Jan. 2021, AIAA 2021: 0421.

[19] Z. Ayers, A.I. Lemcherfi, E. Plaehn, C.D. Slabaugh, T.R. Meyer, C.A. Fugger, S. Roy, Application of 100 kHz acetone-PLIF for the investigation of mixing dynamics in a self-excited linear detonation channel. Scitech 2021 Forum, 11–15 & 19–21 Jan. 2021, AIAA 2021; 0554.

[20] K. Chatelain, R. Mével, J. Melguizo-Gavilanes, A. Chinnayya, S. Xu, D.A. Lacoste, Effect of incident laser sheet orientation on the OH-PLIF imaging of detonations. Shock Waves, In press, https://doi.org/ 10.1007/s00193-020-00963-y

[21] S.B.Rojas Chavez, K.P. Chatelain, T.F. Guiberti, R. Mével, D.A. Lacoste, Effect of the excitation line on hydroxyl radical imaging by laser induced fluorescence in hydrogen detonations, Combust. Flame 2021; 229: 111399.

[22] J. Floyd, P. Geipel, A.M. Kempf, Computed Tomography of Chemiluminescence (CTC): Instantaneous 3D measurements and Phantom studies of a turbulent opposed jet flame, Combust. Flame 2011; 158: 376-391.

[23] T. Yu, C. Ruan, H. Liu, W. Cai, X. Lu, Time-resolved measurements of a swirl flame at 4 kHz via computed tomography of chemiluminescence, Appl. Opt. 2018; 57: 5962-5969.

[24] C. Ruan, T. Yu, F. Chen, S. Wang, W. Cai, X. Lu, Experimental characterization of the spatiotemporal dynamics of a turbulent flame in a gas turbine model combustor using computed tomography of chemiluminescence, Energy 2019; 170: 744-751.

[25] L. Wang, G. Wang, X. Ning, et al. Application of BP neural network to the prediction of coal ash melting characteristic temperature, Fuel 2020; 260: 116324.

[26] L. Zhang, Y. Xue, Q. Xie, Z. Ren. Analysis and neural network prediction of combustion stability for industrial gases. Fuel 2021 287: 119507.

[27] Ö. Böyükdipi, G. Tüccar, H. S. Soyhan. Experimental investigation and artificial neural networks (ANNs) based prediction of engine vibration of a diesel engine fueled with sunflower biodiesel–NH3 mixtures, Fuel 2021; 304: 121462.

[28] J. Huang, H. Liu, W. Cai, Online in situ prediction of 3-D flame evolution from its history 2-D projections via deep learning, J. Fluid Mech. 2019; 875: R2.

[29] K. Malik, M. Żbikowski, A. Teodorczyk, Detonation cell size model based on deep neural network for hydrogen, methane and propane mixtures with air and oxygen, Nucl. Eng. Technol.2019; 51: 424-431.

[30] Y. Zhang, L. Zhou, H. Meng, H. Teng, Reconstructing cellular surface of gaseous detonation based on artificial neural network and proper orthogonal decomposition, Combust. Flame 2020; 212: 156–164.

[31] L. Zhou, H. Teng, H.D. Ng, P.F. Yang, Z.L. Jiang, Reconstructing shock front of unstable detonations based on multi-layer perceptron, arXiv 2021; 2103.12912.

[32] Y. Zhang, L. Zhou, J. Gong, H.D. Ng, H. Teng, Effects of activation energy on the instability of oblique detonation surfaces with a one-step chemistry model, Phys. Fluids. 2018; 30:106110.

[33] E.F. Toro, Riemann Solvers and Numerical Methods for Fluid Dynamics, 3rd ed., Springer, Berlin, Germany, 2009.

[34] H.D. Ng, F. Zhang, Detonation instability, in: F. Zhang (Ed.), Shock Wave Science and Technology Library, Vol. 6, Springer, Berlin, Heidelberg 2012: 107-212.

[35] A.L. Maas, A. Y. Hannun, and A.Y. Ng, Rectifier nonlinearities improve neural network acoustic models, Proc. of the 30th Int. Conf. on Machine Learning 2013; 30 (1): 3.

[36] S. Ioffe, C. Szegedy. Batch normalization: Accelerating deep network training by reducing internal covariate shift, Proc. 32nd International Conference on Machine Learning PMLR 2015; 37: 448-456.

[37] T. Dozat. Incorporating Nesterov Momentum into Adam, Int. Conf. Learning Representations ICLR Workshop, San Juan, Puerto Rico, 2016; May 2-4.

[38] X. Glorot, Y. Bengio. Understanding the difficulty of training deep feedforward neural networks. Proc. 13th International Conference on Artificial Intelligence and Statistics, PMLR 2010; 9: 249-256.